JACS
JOURNAL OF THE AMERICAN CHEMICAL SOCIETY

ARTICLE

pubs.acs.org/JACS

Orientation of Diamagnetic Layered Transition Metal Oxide Particles in 1-Tesla Magnetic Fields

Elizabeth C. Sklute,[†] Miharu Eguchi,[†,⊥] Camden N. Henderson,[†] Mark S. Angelone,[‡] Hemant P. Yennawar,[§] and Thomas E. Mallouk*[,†]

[†]Department of Chemistry, [‡]Materials Research Institute, and [§]Department of Biochemistry and Molecular Biology, The Pennsylvania State University, University Park, Pennsylvania 16802, United States

ABSTRACT: The magnetic field-driven orientation of microcrystals of six diamagnetic layered transition metal oxides ($HLaNb_2O_7$, $HCa_2Nb_3O_{10}\cdot 0.5H_2O$, $KNaCa_2Nb_4O_{13}$, $KTiTaO_5$, $KTiNbO_5$, and $H_{2.2}K_{1.8}Nb_6O_{17}\cdot nH_2O$) suspended in epoxy resins was studied by X-ray diffraction using permanent magnets producing a 0.8 T field. Although the degree of orientation, quantified as the Hermans order parameter, was strongly affected by the particle size distribution, in all cases microcrystals with ~1−2 μm lateral dimensions were found to orient with the magnetic field vector in the layer plane. Control of the orientation of ionically conducting layered oxides is of interest for practical applications in batteries and fuel cells. The consistent direction of orientation of the lamellar oxides studied can be rationalized in the framework of a quantitative bond anisotropy model developed by Uyeda (*Phys. Chem. Miner.* **1993**, *20*, 77−80). The asymmetry of metal−oxygen bonding at the faces of the octahedral layers results in long and short M−O bonds perpendicular to the plane of the sheets. This distortion of the M−O octahedra, which is a structural feature of almost all layered materials that contain octahedral bonding frameworks, gives rise to the diamagnetic anisotropy and results in an easy axis or plane of magnetization in the plane of the sheets.

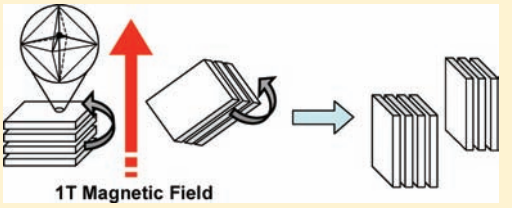

INTRODUCTION

Controlling the orientation of crystals in composite materials is important because it can enhance properties that arise from crystal asymmetry. Lamellar solids, which have strong bonding in two crystallographic directions, are typically very asymmetric in their optical, mechanical, and transport properties. A property that is of particular interest for electrochemical energy conversion in fuel cells and batteries, which often contain layered compounds as electrode or electrolyte materials, is ionic conductivity. Ion-exchangeable layered metal oxides and layered metal phosphates have relatively high proton conductivity,[1−3] and much higher ionic conductivity parallel to the layer plane than they do in the perpendicular direction.[4−7] Membranes and electrode films made from these compounds should thus function more effectively when the direction of highest ionic conductivity is parallel to the anode−cathode axis of the electrochemical cell. Typical deposition methods, however, almost invariably orient lamellar crystallites with their layer planes parallel to the substrate.[5,8] This preferred orientation is driven by surface forces, both in the liquid state and in drying. In order to obtain membranes and films of layered materials with their layer planes perpendicular to the membrane plane, the suspended crystallites should be oriented in solution and then deposited and fixed while maintaining that orientation. Osterloh et al. have shown that the orientation of individual nanosheets can be controlled using magnetic forces, but only after functionalizing them with magnetic nanoparticles.[9−11] We seek to develop a general method for obtaining oriented films and membranes of these materials without the steps of adding and removing magnetic particles.

The magnetic orientation of many diamagnetic materials has been studied using strong magnetic fields.[12−20] Recently, we applied this method to the orientation of lamellar crystals and nanoscrolls derived from layered niobates by applying >10 T magnetic fields.[21,22] Such strong fields, obtained with superconducting magnets, are impractial for the routine preparation of films and membranes. However, it is now easy to realize ~1 T fields with commercially available Nd−Fe−B permanent magnets. This study explores the orientation of layered transition metal oxide particles using a benchtop 0.8 T device made from permanent magnets.

For diamagnetic crystals, the forces controlling orientation are the magnetic field strength, B, the volume of the particle, V, the vacuum permeability, μ_0, and the anisotropy of the diamagnetic susceptibility, $\Delta\chi = \chi_{\parallel} - \chi_{\perp}$, where $\chi_{\parallel}$ and $\chi_{\perp}$ are the magnetic susceptibility parallel and perpendicular to the magnetic principal axis, respectively, such that the energy (U_m) of orientation is

$$U_m = \frac{\Delta\chi V B^2}{2\mu_0} \quad (1)$$

In order to obtain oriented crystals, U_m must exceed the thermal energy, kT. With typical values of $\Delta\chi$, U_m is on the order of kT in 1 T fields for particles in the micrometer size range.[23] Because of the strong dependence of U_m on particle dimensions ($U_m \sim V \sim d^3$), one does not expect diamagnetic nanoparticles to orient in 1 T fields. A key question for the preparation of

Received: August 7, 2010
Published: January 19, 2011

dx.doi.org/10.1021/ja107090n | *J. Am. Chem. Soc.* 2011, 133, 1824–1831

ion-transporting films and membranes from oriented microparticles is the direction of diamagnetic orientation. Interestingly, we find that, for a range of layered oxides, the preferred orientation direction is one in which the magnetic field vector is parallel to the layer plane. This trend is consistent with a bond anisotropy model developed by Uyeda for oxides that contain metals in octahedral or tetrahedral coordination environments.[24−26] Agreement with the predictions of the model for all compounds studied suggests that controlled orientation of microparticles should be achievable with a broad range of layered diamagnetic materials by processing in a ∼1 T magnetic field applied perpendicular to the substrate or sample plane.

EXPERIMENTAL SECTION

Materials Synthesis. Layered niobates, titanates, and tantalates were synthesized by high-temperature solid−solid reactions of mixtures of the appropriate binary oxides and metal carbonates, with 10−20% stoichiometric excess of alkali carbonate to compensate for volatilization. The powders were ground in an agate mortar and pestle, calcined in air in covered alumina crucibles, rinsed with deionized water to remove any excess alkali metal oxide, and then dried in air at 120 °C. $K_4Nb_6O_{17}$ was synthesized from Nb_2O_5 and K_2CO_3 (10% excess) at 1200 °C for 15 min at a ramp rate of 20 °C/min.[21] $RbLaNb_2O_7$ was synthesized from La_2O_3, Nb_2O_5, and Rb_2CO_3 (20% excess) at 1150 °C for 48 h.[27] $KCa_2Nb_3O_{10}$ was synthesized from $CaCO_3$, Nb_2O_5, and K_2CO_3 (20% excess) at 1100 °C for 24 h.[28,29] $KTiNbO_5$ and $KTiTaO_5$ were synthesized from TiO_2 (anatase), Nb_2O_5 or Ta_2O_5, and K_2CO_3 (20% excess) at 1150 for 24 h.[28,30] $KCa_2NaNb_4O_{13}$ was synthesized from $KCa_2Nb_3O_{10}$ and $NaNbO_3$ at 1200 °C for 48 h.[28,31] Sr_2TiO_4 was prepared by the citrate precursor method as described by Nishio et al.[32] Anhydrous strontium chloride (10.0 g) was dissolved in 75 mL of ethanol with dissolved citric acid (14.4 g) as a chelating agent. Glacial acetic acid (8.5 mL) was added to titanium isopropoxide (5.35 mL) to prevent hydrolysis, and then the solution was added to the strontium-containing solution. The solvent was evaporated, and the resulting gel was dried at 500 °C to obtain a precursor powder. The powder was then heated in air three times for 24 h at 1200 °C, grinding the powder after each heating.

Proton Exchange. $K_4Nb_6O_{17}$, $RbLaNb_2O_7$, and $KCa_2Nb_3O_{10}$ were proton-exchanged to obtain $H_{4-x}K_xNb_6O_{17}\cdot nH_2O$ (x = 2.2 by ICP-AES), $HLaNb_2O_7$, and $HCa_2Nb_3O_{10}\cdot 0.5H_2O$ by stirring at room temperature in excess 4 M HNO_3. The solids were filtered, and the acid solution was replaced daily for 3 days or more.[27,28] Upon drying at 120 °C, the hydrated compound $H_{2.2}K_{1.8}Nb_6O_{17}\cdot nH_2O$ (interlayer spacing 9.4 Å) was converted to the anhydrous form (8.0 Å), which rapidly rehydrated in air. In the two-dimensional X-ray diffraction (2D XRD) experiments, the freshly dehydrated material was used and is referred to as $H_{2.2}K_{1.8}Nb_6O_{17}$.

Analysis. XRD analysis was performed on a Philips X'Pert MPD powder X-ray diffractometer (Cu Kα, 40 kV, 40 mA) in $\theta-\theta$ geometry. The patterns were indexed, and lattice parameters were refined using Powder Cell 2.4 and CelRef V3. Particle size distributions were determined by dispersing a powder sample on a glass slide and measuring the average lateral dimensions in images obtained with an Olympus BX60M optical microscope. Particles dispersed in this way tend to orient with their layer plane parallel to the substrate, so the measured sizes represent the average dimensions in the layer plane.

Magnetic Field Orientation of Layered Oxides. Powder samples were suspended in an epoxy resin, which hardened as the crystallites oriented in a magnetic field. In each experiment, 50 mg of the metal oxide powder was ground, dried at 120 °C, and dispersed in 500 mg of bisphenol A-co-epichlorohydrin. The solution was stirred for 12 h at 45 °C to disperse the particles. Next, 100 μL of diethylenetriamine was stirred in for 1 min, and the resulting viscous mixture was injected by pipet into a 1.5 mm × 3.0 mm × 20.00 mm Mylar rectangular mold. One or both ends were sealed with a silicone sealant, and the samples were placed in a static magnetic field of ∼12, ∼7, ∼5, or ∼1 T to cure for 12 h. The ∼12 (11.74 T), ∼7 (7.05 T), and ∼5 T (4.70 T) experiments were done by placing the sample in the bore of an Oxford superconducting magnet in Bruker AMX-2-500 MHz, DPX 300 MHz, and ACE-200 MHz NMR spectrometers, respectively. The ∼1 T field experiments were done by placing the sample between two stacks of axially magnetized cylindrical Nd−Fe−B N40 magnets (0.5 in. diameter × 0.125 in. thickness, remanent magnetization (B_r) 1.25−1.28 T, obtained from Magcraft, Inc.) held apart by a 4 mm aluminum spacer (Figure 1). All samples were cured at ambient temperature. Scanning electron microscopy (SEM) images of these samples were obtained after etching for 1 h in a Novascan PSD-UVT UV-ozone chamber.

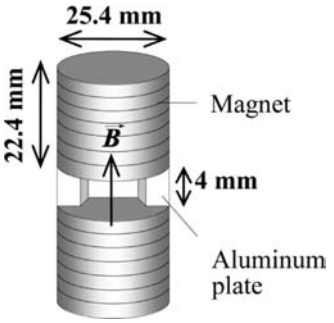

Figure 1. Benchtop magnetic device used to create a ∼1 T static magnetic field. Samples were placed in the cavity with the 3 mm height of the Mylar mold parallel to ***B***.

The magnetic flux density in which the 0.8 T samples were oriented was calculated using the linear combination of the magnetic flux densities at the surface of the cylindrical magnets as described by Furlani:[33]

$$B(z) = B_r\left[\frac{z+L}{\sqrt{(z+L)^2+R^2}} - \frac{z}{\sqrt{z^2+R^2}}\right] \quad (2)$$

where z is the magnetized axis, R is the radius, and L is the length of the magnet stack. For this system, the magnetic flux density was calculated to be 0.91 T at the center of the inter-magnet space (2 mm from each magnet). The magnetic field strength was also measured by using a Magnetic Instrumentation Inc. model 907K gaussmeter, which gave a value of 0.82 T. The difference in field strength can be attributed to deviations from ideal behavior of the magnet stacks acting as individual magnets, since each 22.4 mm segment was composed of combinations of 1/8 in. or 1/4 in. thick discs.

Measurements of particle orientation were made by 2D XRD. Qualitative intensity data were obtained at room temperature on a Bruker SMART APEX CCD area detector system equipped with a graphite monochromator and a Mo Kα fine-focus sealed tube (λ = 0.71073 Å), operated at 1600 W power (50 kV, 32 mA). The detector was placed at a distance of 5.8 cm from the sample. Each frame was collected with an exposure time of 10 s. Quantitative 2D XRD intensity data, used to calculate the orientation parameter of the field-aligned microcrystals, were acquired on a Rigaku D/MAX Rapid II cylindrical image plate detector system with a graphite monochromator and a Mo Kα fine-focus sealed tube (λ = 0.71073 Å), operated at 2000 W power (50 kV, 40 mA). The detector was placed at a distance of 11.4 cm from the sample. Each frame was collected at 2θ = 0, with an exposure time of 20 min. The sample geometry is sketched in Figure 2.

dx.doi.org/10.1021/ja107090n |J. Am. Chem. Soc. 2011, 133, 1824–1831

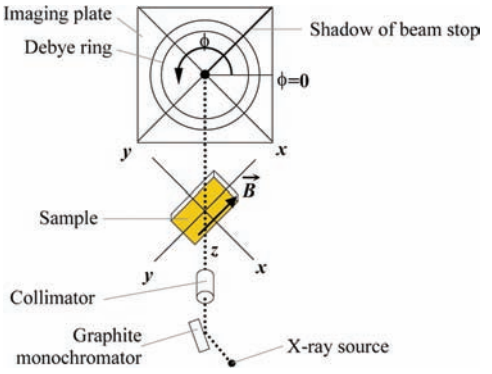

Figure 2. Configuration of the 2D XRD experimental setup. ***B*** is the magnetic field vector.

In this orientation, the $x-y$ plane is parallel to the magnetic field direction, and the incident X-rays are perpendicular to the $x-y$ plane. A crystal positioned in the beam diffracts X-rays into the $x-y$ plane at Bragg angle 2θ. For a sample that consists of many randomly oriented crystals, the diffraction intensity is independent of the azimuthal angle (ϕ), and the diffracted X-rays form a ring of uniform intensity. In contrast, for a single crystal, a Friedel pair of diffraction spots at unique values of 2θ and ϕ, $\phi + 180°$ would be observed, where ϕ depends on the azimuthal orientation of the relevant set of diffracting planes in the crystal. In an oriented polycrystalline sample, spots or arcs are expected in the $x-y$ plane, indicating a preferred orientation with respect to certain crystallographic directions. In the analysis of crystal orientation, low-angle spots and arcs were indexed to the appropriate sets of *hkl* planes (typically planes along the layer axis, as described below) by comparing the 2θ values of the 2D XRD pattern with those in the conventional 1D pattern. The low-angle reflections were used in these experiments as they provide the lowest angle intersection between the Ewald sphere and the plane of preferred orientation. This allows for the detection of the set of poles that deviate the least from the true direction of preferred orientation.

RESULTS AND DISCUSSION

Powder XRD patterns of the layered oxides studied in this work were indexed on the basis of literature reports for $HLaNb_2O_7$,[2] $KTiTaO_5$ and $KTiNbO_5$,[34] $HCa_2Nb_3O_{10}\cdot 0.5H_2O$,[35] and $H_{2.2}K_{1.8}Nb_6O_{17}\cdot nH_2O$.[21] Indexing of $H_{2.2}K_{1.8}Nb_6O_{17}\cdot nH_2O$ was then refined using the known crystal structure of $K_4Nb_6O_{17}$.[36] The crystal structure of $KNaCa_2Nb_4O_{13}$ has not been reported, but its XRD pattern was successfully indexed to a primitive orthorhombic cell by analogy to the known structure of $Na_2Ca_2Nb_4O_{13}$.[37] The indexed XRD patterns are shown in Figure 3, and the lattice constants are given in Table 1.

In our earlier papers, we studied the orientation of acid-exchanged potassium hexaniobate ($H_{2.2}K_{1.8}Nb_6O_{17}\cdot nH_2O$) sheets and nanoscrolls using ~12 T magnetic fields.[21] In those experiments, silica sol−gel chemistry was used to fix the magnetic orientation of the particles for 2D XRD analysis. With the sol−gel, sample drying resulted in cracking, which complicated the quantification of particle orientation. In the experiments reported here, an epoxy resin was used to fix the particle orientation. We examined the same hexaniobate material at three different field strengths (~12, ~5, and ~1 T) as well as five other lamellar oxides in ~1 T magnetic fields and correlated the observed results with calculations of particle diamagnetic anisotropy.

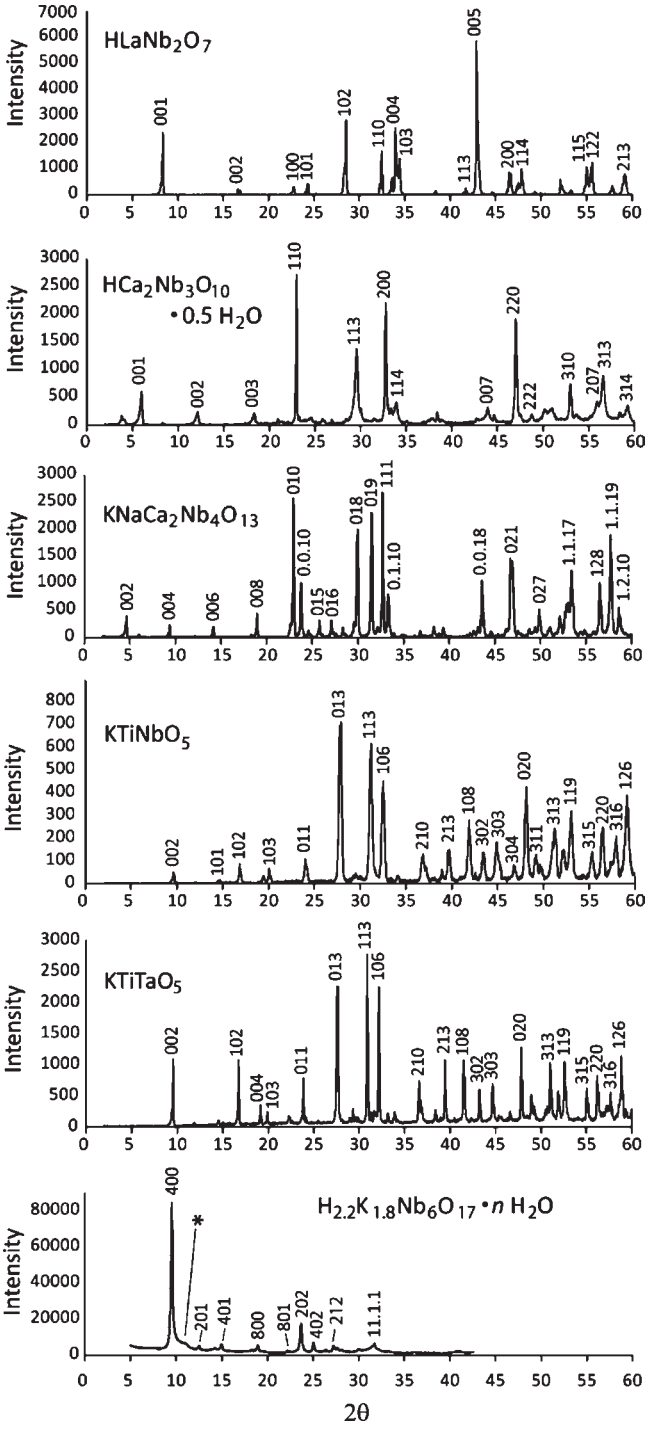

Figure 3. Powder XRD patterns of layered oxides used in this study. The * in the pattern of $H_{2.2}K_{1.8}Nb_6O_{17}\cdot nH_2O$ indicates the position of the (400) reflection of the anhydrous phase.

Figure 4 compares 2D XRD patterns of a polycrystalline sample of $H_{2.2}K_{1.8}Nb_6O_{17}$ oriented at three different field strengths and also shows an SEM image of crystals oriented at high field. Magnetic orientation is evident in all three XRD images as bright spots or arcs on one or more Debye rings. The small bright arcs along the 100 axis, the streaks parallel to 100 in the reciprocal lattice, and the lack of background intensity in the Debye rings in Figure 4a indicate that this sample, including small crystallites

dx.doi.org/10.1021/ja107090n |*J. Am. Chem. Soc.* 2011, 133, 1824–1831

Table 1. Space Groups and Lattice Constants from Powder XRD Patterns of Layered Oxides

compound	space group	layer axis	lattice constant (Å)[a]		
			a	*b*	*c*
$HLaNb_2O_7$	*P*4/*m*	*c*	3.894(7)	3.894(7)	10.511(1)
$HCa_2Nb_3O_{10}\cdot 0.5H_2O$	*P*4/*mbm*	*c*	5.463(10)	5.463(10)	14.456(1)
$KNaCa_2Nb_4O_{13}$	*Pmna*	*c*	3.876(3)	3.885(2)	37.359(16)
$KTiNbO_5$	*Pnma*	*c*	6.418(4)	3.783(2)	18.313(1)
$KTiTaO_5$	*Pnma*	*c*	6.440(2)	3.800(1)	18.482(6)
$H_{2.2}K_{1.8}Nb_6O_{17}\cdot nH_2O$	*Pna*2_1	*a*	37.46(5)	6.658(4)	7.669(9)

[a] Standard deviations are given in parentheses.

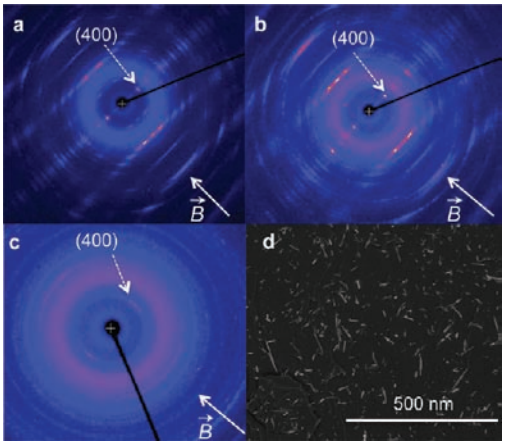

Figure 4. 2D XRD patterns of oriented layered oxide $H_{2.2}K_{1.8}Nb_6O_{17}$ in (a) ~12, (b) ~5, and (c) ~1 T magnetic fields. The magnetic field direction is indicated by the solid arrow. (d) SEM image from the 12 T sample, cleaved along the edge that was perpendicular to the field direction and etched in a UV-ozone chamber. The edges of the oriented crytals are apparent in the image.

in the particle size distribution, is very highly oriented at 12 T. The longer arcs in Figure 4b indicate a lower degree of orientation at 5 T, and at 1 T continuous Debye rings are seen in the pattern (Figure 4c). Clear orientation of the 400 planes can be seen in Figure 4c, however, indicating that even ~1 T magnetic fields are sufficient to achieve preferred orientation of the microcrystals. At all three field strengths, the short arcs of low-angle *h*00 reflections along the field direction indicate that the *a*-axis of the crystal is preferentially oriented perpendicular to the applied magnetic field direction. That is, the magnetic field vector lies in the plane of the tabular microcrystals.

Other layered oxides, $HLaNb_2O_7$, $HCa_2Nb_3O_{10}\cdot 0.5H_2O$, $KNaCa_2Nb_4O_{13}$, $KTiNbO_5$, and $KTiTaO_5$, were then examined to see if a similar preferred orientation would be observed. The structures of these compounds are shown in Figure 5. The first three compounds are layer perovskites in the Dion−Jacobson series with two-, three-, and four-layer $A_{n-1}M_nO_{3n}$ perovskite blocks inter-grown with alkali oxide (AO) or proton-exchanged alkali oxide (HO) layers. $KTiNbO_5$ and $KTiTaO_5$ are shear-structure oxides that contain corrugated sheets of edge- and corner-sharing MO_6 octahedra. All five compounds have low layer charge density and are thus ion-exchangeable. The 2D XRD images of these compounds oriented in 0.8 T fields are shown in Figure 6. In all cases, the lowest-angle arcs correspond to layer lines in the 1D XRD pattern and are polarized along the applied

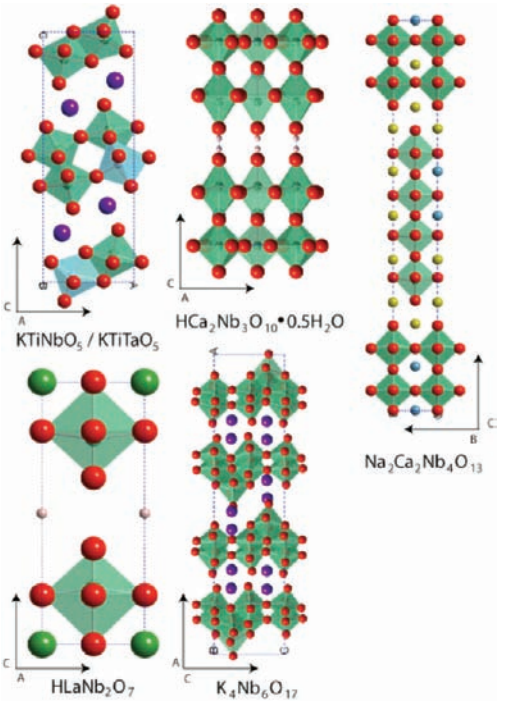

Figure 5. Structures of layered oxide compounds.[2,34−37] In the case of $KNaCa_2Nb_4O_{13}$ and $H_{2.2}K_{1.8}Nb_6O_{17}$, the known structures of $Na_2Ca_2Nb_4O_{13}$ and $K_4Nb_6O_{17}$ are plotted, and their M and O atomic coordinates were used for diamagnetic anisotropy calculations (see below).

field direction. One can thus conclude that powders of these compounds, like $H_{2.2}K_{1.8}Nb_6O_{17}$, orient preferentially with their stacking axis perpendicular to the applied field direction. The *d*-spacings of the lowest-angle layer lines and the crystallographic layer axis directions are summarized in Table 2.

The different compounds studied show varying degrees of orientation, as evidenced by arc intensities, arc lengths, and number of observable preferentially oriented planes (number of arcs visible) in Figure 6. The degree of orientation can be quantified in each case as the Hermans orientation parameter (*f*). This parameter, based on the second-order Legendre function of cos ϕ (where ϕ is the azimuthal angle in a Debye ring) is defined according to eqs 3 and 4. The parameter *f* varies between −1/2 and 1, where values of −1/2, 0, or 1 indicate that a set of diffracting planes (for the relevant Bragg reflection) has a perpendicular, random, or parallel orientation, respectively, with

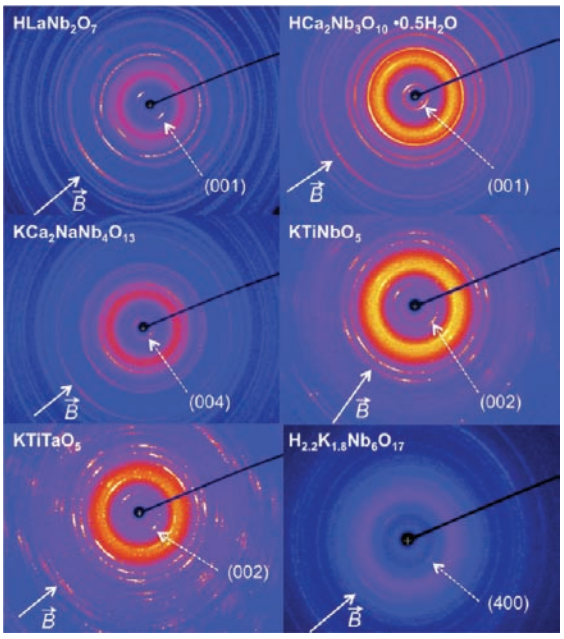

Figure 6. 2D XRD patterns of $HLaNb_2O_7$, $HCa_2Nb_3O_{10}\cdot 0.5H_2O$, $KCa_2NaNb_4O_{13}$, $KTiNbO_5$, $KTiTaO_5$, and $H_{2.2}K_{1.8}Nb_6O_{17}$.

Table 2. Lattice Spacing of Lowest-Angle Layer Line and Crystal Direction of Preferred Orientation from 2D XRD Patterns

compound	*d*-spacing (Å)	crystal plane	orientation	layer axis
$HLaNb_2O_7$	10.5	(001)	⊥ field	*c*
$HCa_2Nb_3O_{10}\cdot 0.5H_2O$	14.6	(001)	⊥ field	*c*
$KNaCa_2Nb_4O_{13}$	9.3	(004)	⊥ field	*c*
$KTiNbO_5$	9.3	(002)	⊥ field	*c*
$KTiTaO_5$	9.4	(002)	⊥ field	*c*
$H_{2.2}K_{1.8}Nb_6O_{17}$	8.0	(400)	⊥ field	*a*

respect to some reference direction.[38] For the samples in this study, the reference orientation in all calculations was $\phi = 0$.

$$\langle \cos^2 \phi \rangle = \int_0^{\pi} \cos^2 \phi \frac{I(\phi)}{\int_0^{\pi} I(\phi) \sin \phi \, d\phi} \sin \phi \, d\phi \quad (3)$$

$$f = \frac{3}{2}\langle \cos^2 \phi \rangle - \frac{1}{2} \quad (4)$$

This calculation was performed in two ways: first by subtracting only the averaged background from the intensity in the diffraction arc, and second by subtracting both the background and the random fraction (or intensity that appears around the remainder of the Debye ring, sampled at $\phi = 90°$). These values, f and f_{rf}, respectively, calculated from the Friedel pair of lowest-angle stacking axis reflections, are listed in Table 3. We hypothesize (see below) that the random fraction consists predominantly of crystallites that are too small to orient in the applied field. The parameter f most accurately describes the orientation of a monodisperse sample of microparticles. For samples that contain a broad range of particle sizes, f_{rf} gives an estimate of the orientation factor of the largest crystallites in the sample.

To calibrate the calculations of f and f_{rf} values, 2D XRD patterns of the $H_{2.2}K_{1.8}Nb_6O_{17}$ sample oriented in ~5 and ~12 T magnetic fields were analyzed. For the ~5 T pattern, subtracting the random fraction increased the order parameter from $f = 0.91$ to $f_{rf} = 0.95$. For the ~12 T pattern, the order parameter increased from $f = 0.94$ to $f_{rf} = 0.99$. These results indicate that there is a relatively small volume fraction of randomly oriented crystallites in these high magnetic fields.

Table 3. Hermans Orientation Parameters (f, f_{rf}) for Samples Cured in Epoxy in ~1 T Magnetic Field

compound	f	f_{rf}	rf[a]
$HLaNb_2O_7$	0.93	0.99	0.06
$HCa_2Nb_3O_{10}\cdot 0.5H_2O$	0.19	0.67	0.48
$KNaCa_2Nb_4O_{13}$	0.31	0.79	0.48
$KTiNbO_5$	0.39	0.85	0.46
$KTiTaO_5$	0.60	0.82	0.22
$H_{2.2}K_{1.8}Nb_6O_{17}$	0.31	0.71	0.40

[a] The random fraction (rf) is calculated as the difference between f and f_{rf}.

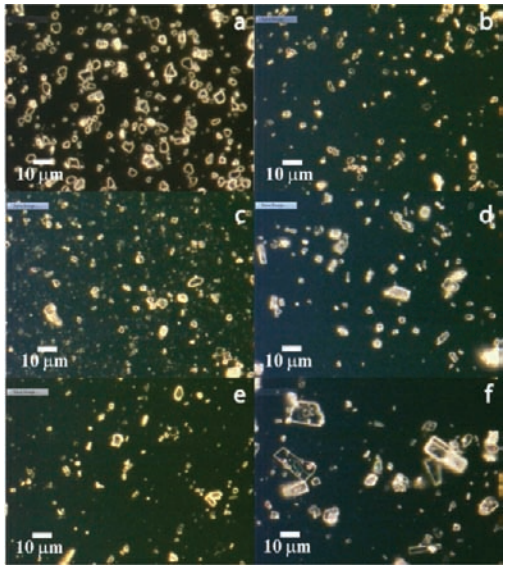

Figure 7. Optical microscope images of (a) $HLaNb_2O_7$, (b) $HCa_2Nb_3O_{10}\cdot 0.5H_2O$, (c) $KNaCa_2Nb_4O_{13}$, (d) $KTiNbO_5$, (e) $KTiTaO_5$, and (f) $H_{2.2}K_{1.8}Nb_6O_{17}\cdot nH_2O$.

For the ~1 T experiments, one of the compounds studied ($HLaNb_2O_7$) showed a low random fraction (6%) and almost complete orientation of the larger crystallites, with f and f_{rf} values above 0.9. In contrast, the other samples had varying random fractions between about 20 and 50%. For these compounds, f_{rf} values ranged from 67 to 85%, indicating that, for each compound, the larger crystallites in the particle size distribution were oriented in the magnetic field (Table 3).

There are several possible reasons why the f_{rf} values for these compounds are significantly lower than that of $HLaNb_2O_7$. Referring to eq 1, the energy U_m that drives the orientation process should be lower for compounds that contain smaller crystallites or have an intrinsically lower diamagnetic anisotropy ($\Delta\chi$). Additionally, viscous or gravitational forces may affect the orientation of larger particles.

The particle size hypothesis was tested by measuring particle size distributions from optical micrographs of the different powder

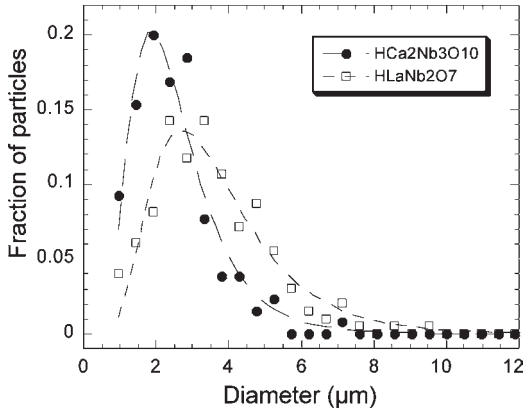

Figure 8. Histograms of average lateral dimensions of powder samples of $HLaNb_2O_7$ and $HCa_2Nb_3O_{10}\cdot 0.5H_2O$ with fits to log-normal distributions.

samples. Representative images are shown in Figure 7. Histograms of particle sizes (taken as the average lateral dimensions of the particles that were large enough to measure accurately) were fit to log-normal distributions. Figure 8 compares particle size distributions for $HLaNb_2O_7$ and $HCa_2Nb_3O_{10}\cdot 0.5H_2O$, which had the highest and lowest f_{rf} values, respectively. The $HLaNb_2O_7$ particle size distribution peaks at a larger value than that of $HCa_2Nb_3O_{10}\cdot 0.5H_2O$, and the latter sample contains a significant part of the distribution below 1 μm.

The particle size distributions obtained from the microscope images can be correlated with the orientation parameters determined by 2D XRD. The materials in which many particles are smaller than 0.5−1 μm (Figure 7b−d) show larger random fractions in the 2D XRD patterns (Figure 6). The ordering of the maxima in particle size distributions was $HLaNb_2O_7 > KTiTaO_5 > H_{2.2}K_{1.8}Nb_6O_{17}\cdot nH_2O \approx KTiNbO_5 \approx KNaCa_2Nb_4O_{13} \approx HCa_2Nb_3O_{10}\cdot 0.5H_2O$, which is consistent with the opposite trend in rf values in Table 3. $H_{2.2}K_{1.8}Nb_6O_{17}\cdot nH_2O$ is an interesting case because it contains small particles that contribute to the random fraction, and also many particles larger than 10 μm. Here, it seems that the viscosity of the setting agent may play an important role. The time-dependent viscosity of the epoxy creates a situation in which, when the setting agent is first added, the epoxy is not viscous enough to suspend the largest particles. Even if the large particles stay suspended, the magnetic torque must overcome the viscous force, which increases linearly with particle size.[38] In either case, for this setting agent, there appears to be an upper limit as well as a lower limit for particle sizes that orient well in a 0.8 T field. Because of this complication, we did not attempt a more detailed analysis to fit the particle size distribution with the 2D XRD results. Given the correspondence between the presence of small particles and large random fractions, it is reasonable to use f_{rf} as the approximate order parameter of the particles at the high end of the size distribution that have sufficient volume to orient in the 0.8 T magnetic field.

Previous reports by Uyeda and co-workers support the correlation between orientation of micrometer-sized particles in magnetic fields and particle size.[24,39] However, related studies have shown that similarly sized particle suspensions of different materials require different field strengths in order for U_m to exceed kT.[26] Uyeda et al. concluded that for tetrahedral sheet silicates, as well as certain octahedral metal oxides, the magnetic

Table 4. Literature Crystal Structures Used for $\Delta\chi$ Calculations

compound	space group	layer axis	lattice constant (Å) a	b	c	ref
$HLaNb_2O_7$	$P4/m$	c	3.8886	3.8886	10.548	31
$HCa_2Nb_3O_{10}\cdot 0.5H_2O$	$P4/mbm$	c	5.452	5.452	14.414	35
$Na_2Ca_2Nb_4O_{13}$	$Immm$	c	3.885	3.884	36.360	37
$KTiNbO_5$	$Pnma$	c	6.447	3.797	18.431	34
$KTiTaO_5$	$Pnma$	c	6.437	3.797	18.474	34
$K_4Nb_6O_{17}$	$Pna2_1$	a	33.210	6.460	7.830	36

orientation was governed primarily by diamagnetic anisotropy and further showed a quantitative correlation between orientation and calculated diamagnetic anisotropy values.[26] The idea that the diamagnetic anisotropy of a crystal can be taken as a sum over individual bond contributions follows from the Langevin−Debye formulation of diamagnetism, which predicts that the average radius squared of an electron orbital is proportional to its diamagnetic susceptibility in the bonding direction.[40,41] Following Uyeda, the energy of an individual M−O bond in a magnetic field is given as

$$U(B) = -(1/2)B^2\{\chi_{MO\perp} + \Delta\chi_{MO}\{(a^2\alpha^2 + b^2\beta^2 + c^2\gamma^2)\} \quad (5)$$

where $\Delta\chi_{MO} = \Delta\chi_{MO||} - \chi_{MO\perp}$ is the diamagnetic anisotropy of the bond, α, β, and γ are the M−O bond direction cosines along the a, b, and c crystallographic directions, and α, β, and γ are the direction cosines of the magnetic field vector. To obtain the diamagnetic anisotropy of the crystal, the contributions of the individual bonds are summed, and differences in these sums are calculated according to eqs 6−8:[24,42]

$$\Delta\chi[x-y] = \Delta\chi_{MO}(\sum\alpha^2 - \sum\beta^2) \quad (6)$$

$$\Delta\chi[y-z] = \Delta\chi_{MO}(\sum\gamma^2 - \sum\beta^2) \quad (7)$$

$$\Delta\chi[z-x] = \Delta\chi_{MO}(\sum\gamma^2 - \sum\alpha^2) \quad (8)$$

Although the value of $\Delta\chi_{MO}$ is unknown, empirically Uyeda found that for a range of octahedral Al and Mg oxides,

$$\Delta\chi = (-0.19\Delta\sum + 0.03) \times 10^{-6}\ \text{emu/mol} \quad (9)$$

where $\Delta\sum$ represents the absolute value of the difference $(\sum\alpha^2 - \sum\beta^2)$, $(\sum\gamma^2 - \sum\beta^2)$, or $(\sum\gamma^2 - \sum\alpha^2)$.

To calculate $\Delta\chi$ values from eq 9 for the octahedral oxides studied here, atomic coordinates were taken from the crystal structure, or in the case of unknown structures, from an analogous compound with the same M−O octahedral bonding framework (see Table 4). Thus, for $Na_2Ca_2Nb_4O_{13}$, Nb and O coordinates were taken from the structure of $KNaCa_2Nb_4O_{13}$, and coordinates from $K_4Nb_6O_{17}$ were used for $H_{2.2}K_{1.8}Nb_6O_{17}$. Sums of α^2, β^2, and γ^2 were calculated over the unit cell (i.e., over $Z \times$ (no. metal atoms per formula unit) $\times$ 6 M−O bonds), and the result was divided by the number of formula units per cell (Z) to obtain molar values. It was assumed that the octahedral M−O contribution to $\Delta\chi$ was much larger than that of H−O or alkali−O bonds, as shown in previous studies,[38,39] and thus contributions

dx.doi.org/10.1021/ja107090n |J. Am. Chem. Soc. 2011, 133, 1824–1831

Table 5. Direction Cosine Sums and $\Delta\chi$ Values[a]

compound	$\sum\alpha^2$	$\sum\beta^2$	$\sum\gamma^2$	$\lvert\chi[y-x]\rvert$	$\lvert\chi[y-z]\rvert$	$\lvert\chi[x-z]\rvert$	easy axis or plane
$HLaNb_2O_7$	3.9166	3.9166	4.1695	–	0.08	0.08	$a-b$ plane
$HCa_2Nb_3O_{10}\cdot 0.5H_2O$	3.8980	3.8980	4.2040	–	0.09	0.09	$a-b$ plane
$Ca_2Na_2Nb_4O_{13}$	7.8758	7.8664	8.2578	0.03	0.10	0.10	$a-b$ plane
$KTiNbO_5$	4.0731	3.6095	4.3174	0.12	0.16	0.08	b-axis
$KTiTaO_5$	4.3882	3.5337	4.0781	0.19	0.13	0.08	b-axis
$K_4Nb_6O_{17}$	12.4978	12.0532	11.4489	0.12	0.15	0.23	c-axis

[a] $|\Delta\chi|$ are in units of 10^{-6} emu/mol.

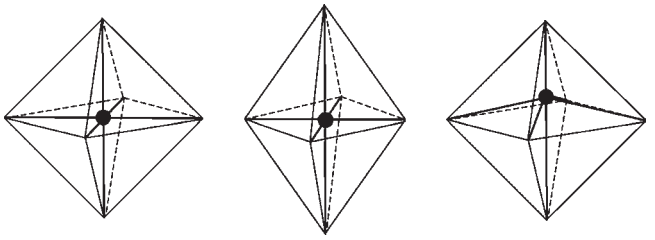

Figure 9. A regular MO_6 octahedron (left), a tetragonally distorted octahedron with D_{4h} symmetry (center), and a tetragonally distorted octahedron with C_{4v} symmetry, in which the metal atom is displaced along the 4-fold axis (right).

from these bonds were neglected. The results of these calculations are shown in Table 5.

It should be noted that the sign of the diamagnetic force, which opposes the applied magnetic field, should always be negative. The diamagnetic anisotropy is defined as $\Delta\chi = \chi_{\parallel} - \chi_{\perp}$, where $\chi_{\parallel}$ and $\chi_{\perp}$ are the susceptibilities parallel and perpendicular to the diamagnetic principal axis, which is the axis that, when collinear with the magnetic field vector, minimizes the energy. It follows that $|\chi_{\parallel}| < |\chi_{\perp}|$, and thus $\Delta\chi$ and U_m are always positive. For this to be true, $\Delta\sum$ must be negative, which is the sign convention adopted here (see Table 5). It is, therefore, apparent that the smallest of the sums ($\sum\alpha^2$, $\sum\beta^2$, and/or $\sum\gamma^2$) should correspond with the easy axis or easy plane, which orients parallel to the applied magnetic field direction.

No obvious correlation between the magnitude of $\Delta\chi$ and the orientation parameter f_{rf} emerges from these data. This is not unexpected, given the narrow range of $\Delta\chi$ and the errors noted above in obtaining f_{rf} from samples that contain a broad distribution of particle sizes. What is striking, however, is the consistent direction of preferred orientation. In each case, the calculated order of $\Delta\chi$ values agrees with the observed preferred orientation of the lamellar crystallites in the magnetic field. The direction of preferred orientation is the same for the two-, three-, and four-layer perovskites $HLaNb_2O_7$, $HCa_2Nb_3O_{10}\cdot 0.5H_2O$, and $KNaCa_2Nb_4O_{13}$, in which the covalent M−O bonding framework consists of corner-sharing octahedra, and for shear structure oxides $HTiMO_5$ (M = Nb, Ta) and $H_{2.2}K_{1.8}Nb_6O_{17}$ that contain corrugated planes of edge- and corner-sharing octahedra. Uyeda and co-workers have also previously noted this direction of orientation for $Al(OH)_3$ and $Mg(OH)_2$ crystals, which contain planes of edge-sharing octahedra,[24] and for layered silicates that contain similar octahedral sheets bonded to tetrahedral $[Si_2O_5]_n^{2n-}$ layers.[26]

It is interesting to consider which structural feature(s) of layered solids should cause the easy axis or plane of magnetization to lie consistently in the layer planes. It is apparent from eqs 5−9 that a regular MO_6 octahedron, regardless of its orientation, should not possess diamagnetic anisotropy. This is also true for a tetragonally distorted octahedron that retains its center of symmetry, as illustrated in Figure 9. In both cases, the sum of the squares of the bond direction cosines is the same along all three Cartesian axes, and $\Delta\sum$ in eq 9 is zero. Thus, according to the bond anisotropy model, cooperative tilting of regular octahedra, as occurs in many layer perovskite structures, or simple tetragonal distortions should not induce diamagnetic anisotropy. However, if the center of symmetry of the octahedron is removed, for example by displacing the metal ion from the center, then $\Delta\sum$ becomes nonzero. In the C_{4v} symmetry example shown in Figure 9, the metal is displaced along the z-axis, and the equatorial M−O bonds acquire a non-zero z-axis component. It follows in this case that $\Delta\gamma^2 > \Delta\alpha^2, \Delta\beta^2$, so the easy axis should be perpendicular to z.

In layered materials, the asymmetry of the bonding network invariably distorts MO_6 octahedra. In some cases, such as single-layer perovskites (for example, Sr_2TiO_4),[43,44] the distorted octahedron has D_{4h} symmetry, and there should be no diamagnetic anisotropy. This prediction was borne out by 2D XRD patterns of Sr_2TiO_4 microcrystals cured in epoxy resin in a 7 T field. These patterns showed no preferred orientation and were essentially identical to patterns of samples prepared in zero field. However, for higher-order layer perovskites as well as for shear structure oxides, the intergrowth of ionic and covalent structures creates asymmetry of M−O bonding along the layer axis, resulting in displacement of metal atoms along that direction. For example, in $HLaNb_2O_7$, the Nb−O bond pointing into the layer gallery is shorter than that bridging to a Nb atom in the second octahedral layer. In $HCa_2Nb_3O_{10}\cdot 0.5H_2O$, the octahedral layers facing the galleries have the same kind of distortion, but Nb atoms in the middle layer of the perovskite blocks are in a centrosymmetric MO_6 environment. Thus, only the former contribute to the diamagnetic anisotropy of $HCa_2Nb_3O_{10}\cdot 0.5H_2O$. It is important to note that structures such as Sr_2TiO_4, in which none of the MO_6 octahedra have diamagnetic anisotropy, are rather rare among layered oxides. In general, we can expect the M−O bonding asymmetry along the layer axis to create anisotropy that will lead to orientation in applied magnetic fields.

■ CONCLUSIONS

We have found with six different ion-exchangeable layered oxide structures that microcrystals can be oriented in suspensions by a 0.8 T static magnetic field. This result is significant because such fields can be easily attained in the laboratory or even in a manufacturing environment by using permanent magnets. Thus, it may be possible to process diamagnetic materials that have highly anisotropic proton or lithium ion conductivities into optimally

oriented membranes or electrodes by this technique. We find, in all cases, the same preferred orientation of the crystallites, which can be rationalized in terms of long−short M−O bond asymmetry in the direction of the layer axis. Calculations of the molar diamagnetic anisotropy $\Delta\chi$ gave a relatively narrow range ($0.08-0.23 \times 10^{-6}$) for the materials studied, consistent with previous measurements of $\Delta\chi$ for octahedral solids.[24] Of the materials studied, $HLaNb_2O_7$, which had a narrow distribution of particle sizes centered about 2 μm, gave the highest value of Hermans orientation factors f and f_{rf}. This result, which is consistent with the strong dependence of the magnetic energy on particle size, suggests that particle separation techniques based on size could serve to increase the degree of preferred orientation of lamellar oxides.

AUTHOR INFORMATION

Corresponding Author

tem5@psu.edu

Present Addresses

[⊥]Graduate School of Pure and Applied Sciences, University of Tsukuba, 1-1-1 Tennodai, Tsukuba, Ibaraki 305-8571, Japan

ACKNOWLEDGMENT

This work was supported by the National Science Foundation under grant CHE-0910513. We thank Dr. Alan Benesi for his help with diamagnetic orientation experiments performed using NMR magnets.

REFERENCES

(1) Thangadurai, V.; Shukla, A. K.; Gopalakrishnan, J. *Solid State Ionics* **1994**, *73*, 9–14.

(2) Sato, M.; Abo, J.; Jin, T.; Ohta, M. *J. Alloys Compd.* **1993**, *192*, 81–83.

(3) Thangadurai, V.; Weppner, W. *Solid State Ionics* **2004**, *174*, 175–183.

(4) Sudworth, J. L.; Barrow, P.; Dong, W.; Dunn, B.; Farrington, G. C.; Thomas, J. O. *MRS Bull.* **2000**, *25*, 22–26.

(5) Alberti, G.; Casciola, M.; Costantino, U.; Leonardi, M. *Solid State Ionics* **1984**, *14*, 289–295.

(6) Schottenfeld, J. A.; Kobayashi, Y.; Wang, J.; Macdonald, D. D.; Mallouk, T. E. *Chem. Mater.* **2008**, *20*, 213–219.

(7) Howe, A. T.; Shilton, M. G. *J. Solid State Chem.* **1979**, *28*, 345–361.

(8) Alberti, G.; Casciola, M. *Annu. Rev. Mater. Res.* **2003**, *33*, 129–154.

(9) Kim, J. Y.; Osterloh, F. E.; Hiramatsu, H.; Dumas, R. K.; Liu, K. *J. Phys. Chem. B* **2005**, *109*, 11151–11157.

(10) Liu, K.; Zhao, L.; Klavins, P.; Osterloh, F. E.; Hiramatsu, H. *J. Appl. Phys.* **2003**, *93*, 7951–7953.

(11) Osterloh, F. E. *J. Am. Chem. Soc.* **2002**, *124*, 6248–6249.

(12) Sarkar, P.; Nicholson, P. S. *Appl. Phys. Lett.* **1992**, *61*, 492–494.

(13) Suzuki, T. S.; Sakka, Y.; Kitazawa, K. *Adv. Eng. Mater.* **2001**, *3*, 490–492.

(14) Yamato, M.; Aoki, H.; Kimura, T.; Yamamoto, I.; Ishikawa, F.; Yamaguchi, M.; Tobita, M. *Jpn. J. Appl. Phys. Pt. 1* **2001**, *40*, 2237–2240.

(15) Lemaire, B. J.; Davidson, P.; Ferre, J.; Jamet, J. P.; Petermann, D.; Panine, P.; Dozov, I.; Jolivet, J. P. *Eur. Phys. J. E* **2004**, *13*, 291–308.

(16) Uchikoshi, T.; Suzuki, T. S.; Okuyama, H.; Sakka, Y. *J. Mater. Res.* **2003**, *18*, 254–256.

(17) Uchikoshi, T.; Suzuki, T. S.; Okuyama, H.; Sakka, Y.; Nicholson, P. S. *J. Eur. Ceram. Soc.* **2004**, *24*, 225–229.

(18) Uchikoshi, T.; Suzuki, T. S.; Tang, F.; Okuyama, H.; Sakka, Y. *Ceram. Int.* **2004**, *30*, 1975–1978.

(19) Kimura, T.; Yoshino, M. *Langmuir* **2005**, *21*, 4805–4808.

(20) Kimura, T.; Kimura, F.; Yoshino, M. *Langmuir* **2006**, *22*, 3464–3466.

(21) Eguchi, M.; Angelone, M. S.; Yennawar, H. P.; Mallouk, T. E. *J. Phys. Chem. C* **2008**, *112*, 11280–11285.

(22) Ida, S.; Ogata, C.; Eguchi, M.; Youngblood, W. J.; Mallouk, T. E.; Matsumoto, Y. *J. Am. Chem. Soc.* **2008**, *130*, 7052–7059.

(23) Kimura, T.; Uemura, T.; Takagi, S.; Inoue, H. *Macromol. Symp.* **2006**, *242*, 120–125.

(24) Uyeda, C.; Tanaka, K. *J. Phys. Soc. Jpn.* **2003**, *72*, 2334–2337.

(25) (a) Uyeda, C.; Takeuchi, T.; Yamagishi, A.; Tsuchiyama, A.; Yamanaka, T.; Date, M. *Phys. Chem. Miner.* **1993**, *20*, 369–374. (b) Uyeda, C. *Jpn. J. Appl. Phys.* **1993**, *32*, L268–L270.

(26) Uyeda, C. *Phys. Chem. Miner.* **1993**, *20*, 77–81.

(27) Kobayashi, Y.; Schottenfeld, J. A.; Macdonald, D. D.; Mallouk, T. E. *J. Phys. Chem. C* **2007**, *111*, 3185–3191.

(28) Fang, M. M.; Kim, C. H.; Mallouk, T. E. *Chem. Mater.* **1999**, *11*, 1519–1525.

(29) Dion, M.; Ganne, M.; Tournoux, M. *Mater. Res. Bull.* **1981**, *16*, 1429–1435.

(30) Wadsley, A. D. *Acta Crystallogr.* **1964**, *17*, 623–&.

(31) (a) Jacobson, A. J.; Johnson, J. W.; Lewandowski, J. T. *Inorg. Chem.* **1985**, *24*, 3727–3729. (b) Sato, M.; Abo, J.; Jin, T.; Ohta, M. *J. Alloys Compd.* **1993**, *192*, 81–83.

(32) Nishio, K.; Fukuda, K.; Imai, T.; Takenouchi, H.; Mae, H.; Fujimoto, M.; Iida, T.; Hamada, N.; Kineri, T.; Watanabe, T. *Mater. Res. Soc. Symp. Proc.* **2008**, *1044*, 1044–U06–03.

(33) Furlani, E. *Permanent Magnet and Electromechanical Devices: Materials, Analysis, and Applications*; Academic Press: San Diego, CA, 2001; p 130.

(34) Rebbah, H.; Desgardin, G.; Raveau, B. *J. Solid State Chem.* **1980**, *31*, 321–328.

(35) Chen, Y. F.; Zhao, X. H.; Ma, H.; Ma, S. L.; Huang, G. L.; Makita, Y. J.; Bai, X. D.; Yang, X. J. *J. Solid State Chem.* **2008**, *181*, 1684–1694.

(36) Gasperin, M.; LeBihan, M. T. *J. Solid State Chem.* **1982**, *43*, 346–353.

(37) Chiba, K.; Ishizawa, N.; Nagai, Y.; Oishi, S. *Solid State Ionics* **1998**, *108*, 179–183.

(38) Kimura, T. *Polym. J.* **2003**, *35*, 823–843.

(39) Uyeda, C.; Takeuchi, T.; Yamagishi, A.; Date, M. *J. Phys. Soc. Jpn.* **1991**, *60*, 3234–3237.

(40) Vleck, J. H. V. *The Theory of Electric and Magnetic Susceptibilities*; 1st ed.; Oxford University Press: London, 1932; p 207.

(41) Pauling, L. *J. Chem. Phys.* **1936**, *4*, 673–677.

(42) Uyeda, C.; Ohtawa, K.; Okita, K.; Uyeda, N. *J. Phys. Soc. Jpn.* **2001**, *70*, 889–892.

(43) Ruddlesden, S. N.; Popper, P. *Acta Crystallogr.* **1957**, *10*, 538–540.

(44) Ruddlesden, S. N.; Popper, P. *Acta Crystallogr.* **1958**, *11*, 54–55.